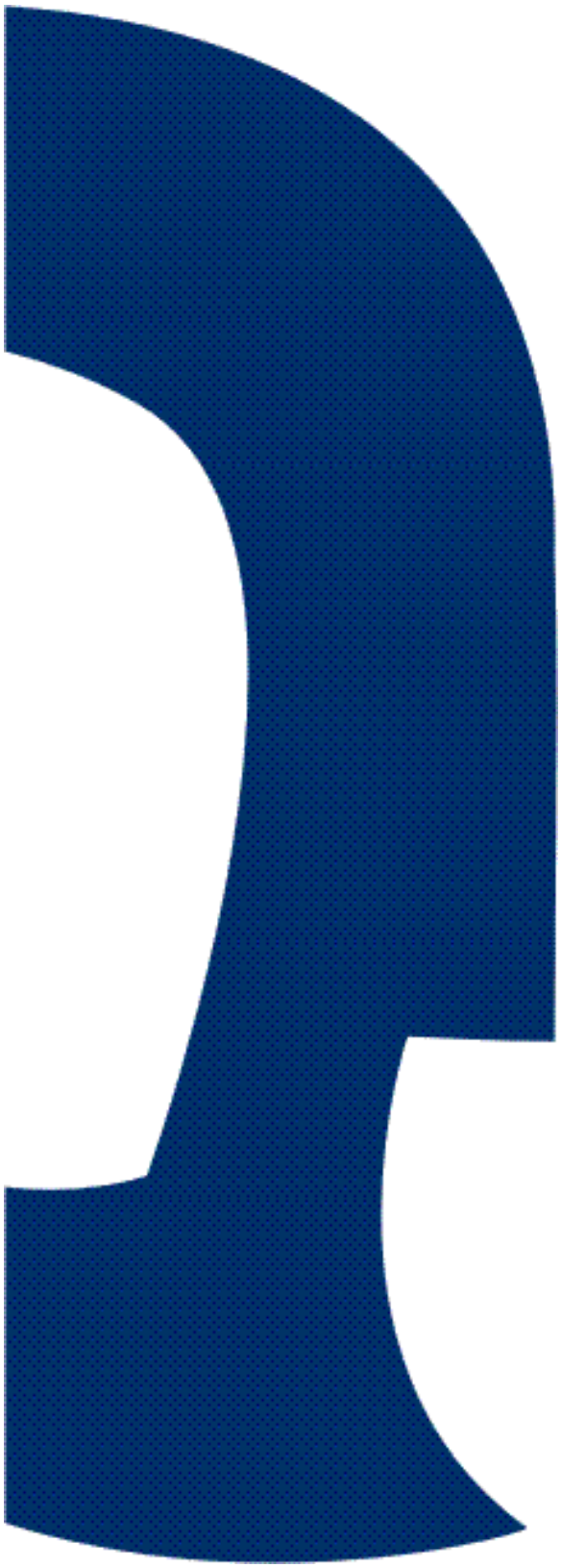

FACULTAD DE CIENCIAS DEL MAR

UNIVERSIDAD DE LAS PALMAS DE GRAN CANARIA

# Exploring hydrographical structures in the Cape Verde Frontal Zone through gliders during FLUXES-II survey

**Inés Hernández García**

**Curso 2018/2019**

**Dr. Francisco José Machín Jiménez**

**Dr. Josep Coca Sáez de Albéniz**

Trabajo Fin de Título para la obtención del título del Máster Universitario en Oceanografía

# Exploring hydrographical structures in the Cape Verde Frontal Zone through gliders during FLUXES-II survey

Trabajo de fin de título presentado por Inés Hernández García para la obtención del título de Máster Universitario en Oceanografía por la Universidad de Las Palmas de Gran Canaria, la Universidad de Vigo y la Universidad de Cádiz.

Tutor: Dr. Francisco José Machín Jiménez, Departamento de Física (Universidad de Las Palmas de Gran Canaria), Grupo de Investigación OFYGA

Co-tutor: Dr. Josep Coca Sáez de Albéniz, División de Robótica y Oceanografía Computacional (ROC) IUSIANI-ULPGC

Estudiante: Tutores:

Inés Hernández García Francisco José Machín Jiménez Josep Coca Sáez de Albéniz

Las Palmas de Gran Canaria, a 5 de julio de 2019

# Table of contents

# 1. Abstract and keywords

## Abstract

The Cape Verde Frontal Zone (CVFZ) is a dynamically complex region located at the eastern North Atlantic Subtropical Gyre (20ºW to 30ºW, ~20ºN), where the warmer and more saline North Atlantic Central Water (NACW) and the colder and less saline South Atlantic Central Water (SACW) interact. It is defined by the intersection of the 36.0 isohaline with the 150 m depth isobath. It is subjected to high variability, with the presence of lateral intrusions, filaments from the upwelling system and mesoscale and submesoscale eddy fields with a sharp thermohaline gradient. Temperature decrease compensates the salinity decrease with depth, so both variables compensate their effect on density, making the front dynamically stable.

The aim of this project is to analyse the features at the CVFZ during November 2017 using the *in situ* FLUXES-II data, obtained from ship CTD stations, a SeaSoar and two deep gliders with biochemical and dynamical instruments.

Data and Copernicus Mercator model outputs were compared to determine their skills to capture the mesoscale and submesoscale features. The variables used on this study were potential temperature, practical salinity, potential density and oxygen concentration.

Wavelet analyses were conducted to compare the different scales that can be accessed with the sampling methods. It allows to determine the main wavelengths in the signal, using distance as the independent variable rather than time.

Results showed that the ship CTD data reaches the greatest depth of all the sampling methods and the SeaSoar is the fastest method. The glider and the SeaSoar capture the smallest scales and show the features with greater detail, while the glider has a slightly better resolution.

## Keywords

Cape Verde Frontal Zone, water masses, Autonomous Underwater Vehicles (gliders). Remotely Operated Vehicles (SeaSoar), numerical models, wavelet analysis, mesoscale and submesoscale features.

## 2. Introduction

The Cape Verde Frontal Zone (CVFZ) is a dynamically complex region located at the eastern North Atlantic Subtropical Gyre. This front is defined by two main water masses at surface and central levels in the North Atlantic Ocean (North Atlantic Central Water, NACW, and South Atlantic Central Water, SACW), showing strong interleaving in the region (Tomczak Jr, 1981; Barton, 1987; Zenk *et al*., 1991; Pérez-Rodríguez *et al*.; 2001; Martínez-Marrero *et al*., 2008; Pelegrí *et al*., 2017).

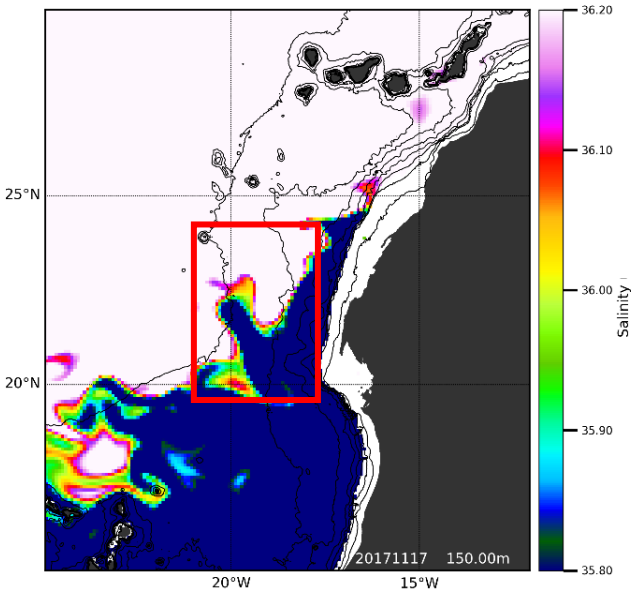


**Figure 1: Location of the CVFZ, reported by the 36 isohaline at 150 m. The red square shows the area sampled by the FLUXES-II survey. The grey contour lines indicate the bathymetry. The map was made using global Mercator model data at 150 m, at November 17th.**

NACW is defined by an almost linear relationship between temperature and salinity in the range 11-18.65 ºC and 35.47-36.76, while SACW does so in the range 9.7-15.25 ºC and 35.177-35.7. SACW is also featured by a minimum in oxygen (Tomczak Jr, 1981; Hagen, 1985; Zenk *et al*., 1991). Below those water masses, Antarctic Intermediate Water (AAIW) can be observed, featured by a minimum in both salinity and oxygen (Pérez *et al*., 2001; Bashmachnikov *et al*., 2015).

The front is defined by the intersection of the 36.0 isohaline with the 150 m depth isobath (Barton, 1987; Zenk *et al*., 1991). It is present throughout the year extending from 20ºW to 30ºW at latitudes close to 20ºN (Mittelstaedt, 1983; Tomczak Jr and Hughes, 1980). It is subjected to high spatial and temporal variability (Barton, 1987; Tomczak Jr, 1981; Zenk *et al*., 1991; Martínez-Marrero *et al*., 2008).

This strong meandering thermohaline front is characterized by the presence of intrusions, filaments from the upwelling system and eddy activity. It shows sharp gradients in

temperature (<3ºC) and salinity (<0.08) in depths up to 600 m. Temperature decrease with depth is large enough to compensate the salinity decrease with depth, so both variables compensate their effect on density making the front dynamically stable (Hughes and Barton, 1974; Barton, 1987; Zenk *et al*., 1991; Pérez-Rodríguez *et al*., 2001; Martínez-Marrero *et al*., 2008).

Gliders have emerged during the last decades and have a huge range of applications in oceanography. They can dive up to 1000 m depth and travel during long periods (up to months), due to their low-battery consumption. They move by changing their buoyancy and using their wings to produce forward upward and downward motions. Gliders take near real time measurements and can access ocean areas that cannot be sampled by oceanic ships in the context of long-distance missions (Rudnick *et al*., 2004; Bachmayer *et al*., 2004; Bachmayer *et al.*, 2006, Hernández-García *et al*., 2018; Ramos *et al*., 2018).

The aim of this project is to describe the features at the CVFZ during November 2017 using the in situ FLUXES-II data and Copernicus Mercator Model outputs, comparing several sampling methods to determine their skills to capture the features at this area with a pronounced spatial and temporal variability.

# 3. Data and methods

## 3.1. FLUXES-II

The FLUXES-II cruise was developed at the CVFZ between November 2nd, 2017 and November 24th, 2017, using the BIO Sarmiento de Gamboa. One of the main objectives of the FLUXES project was to study the hydrographic characteristics of the front. CTD stations, SeaSoar, glider, ADCP and turbulence measurements were made, among others (Martínez-Marrero *et al.*, 2017).

## 3.2. Data sources

On this study we focus on the ship CTD stations, SeaSoar and glider measurements, in addition to the Mercator model output.

### 3.2.1. Mercator model

The model is taken from the Copernicus Marine Environment Monitoring Service (CMEMS, http://marine.copernicus.eu, dataset GLOBAL_ANALYSIS_FORECAST_PHY_001_024). It is a numerical forecasting model with daily outputs (von Schuckmann *et al*., 2016). The dataset finally used is extracted from the model at the same locations and dates of the glider data. It has a horizontal resolution of 1/12º (0.083º) and 50 vertical levels, from the sea surface to 5500 m depth.

### 3.2.2. Ship CTD

48 stations were made using the CTD equipped on the rosette, 36 of them being used on this project, between November 11th and November 20th. It took measurements from the sea surface down to 1500 m depth. The stations were separated 9.26 km. The vertical resolution is approximately 1 m (Martínez-Marrero *et al*., 2017).

### 3.2.3. SeaSoar

The SeaSoar travels in a path of continuous tows dragged by the ship. The chosen transect for this study is the T5 from the FLUXES-II project, done between November 8th and November 9th. It measured the water column from the surface to approximately 450 m depth. It has a horizontal resolution of approximately 2.5 km and a vertical resolution of 0.5 m (Martínez-Marrero *et al.*, 2017).

### 3.2.4. Gliders

Gliders are Autonomous Underwater Vehicles (AUVs). They change their buoyancy to move on the water column and produce forward motion, besides using the ocean currents to help their movement. They were deployed between November 4th and November 21st. They travelled from the surface to 1000 m, for more than 350 km. The gliders deployed were Bio-584 and Dyna-585. During this mission, Bio and Dyna travelled at approximately 20 cm/s following the same path, straight ahead the biochemical path sampled by the ship. For this study the data from Bio was used, since it provides similar results as Dyna and Bio was measuring additional biochemical data (oxygen concentration). The datasets have a horizontal ground resolution of approximately 1 km and a vertical resolution of approximately 1 m (Bachmayer *et al.*, 2006; Martínez-Marrero *et al.*, 2017).

## 3.3. Data processing

The variables used on this study are potential temperature, practical salinity, potential density and oxygen. All the data were processed using Matlab.

### 3.3.1. Wavelet analysis

On this study we use the wavelet analysis to compare the different scales that can be accessed with the sampling methods. The wavelet analysis is a technique used to decompose a time series into a time-frequency space, allowing us to determinate the main frequencies of the signal. It provides an easily interpretable visual representation of the signals, showing a local value for the amplitude and phase for each harmonic of a dataset. Thus, wavelets are useful to describe non-stationary processes that cannot be detected by the classical Fourier Transform technique. Fourier analysis fails when a signal is non-periodic, and the scale properties are time dependent. Wavelet analysis can be applied to

signals of any size, while Fourier Transform requires a given size (Combes *et al*., 2012; Meyers *et al*.1993; Weng and Lau, 1994; Lau and Weng, 1995; Baliunas *et al*., 1997; Torrence and Compo, 1998; Venkata-Ramana *et al*. 2013).

Wavelet analysis was introduced by Morlet *et al*. (1982), Morlet (1983) and Grossman and Morlet (1984) and has been largely used in climatic studies (Kumar and Foufoula-Georgiou, 1993; Gao and Li, 1993; Gollmer *et al*., 1995; Gu and Philander, 1995; Wang & Wang, 1996; Baliunas *et al*., 1997), seismic signals (Baker, 2007), medical research, image processing and the study of flow and waves patterns in the ocean (Farge, 1992; Meyers *et al*., 1993; Liu, 1994), among others (Lau and Weng, 1995; Torrence and Compo, 1998).

In this study, it has been used the complex continuous Morlet wavelet method. A complex wavelet allows us to detect amplitude and phase (imaginary and real parts). Orthogonal wavelets are more useful for decomposition and reconstruction of signals, while continuous wavelets are more useful for scale analysis. However, continuous wavelets, on the other hand, can be redundant on bigger scales (Lau and Weng, 1995; Torrence and Compo, 1998).

# 4. Results and discussion

## 4.1. TS Diagram and Water Masses

Figure 2 shows the TS diagram during the cruise, made with the CTD data taken from the ship. The main water masses found are NACW and SACW. SACW is slightly less saline and colder than the NACW located at the same depth. The surface data shows the highest variability, due to insolation during summer and autumn, and the possible effect of the water exported in filaments from the African upwelling system. Some mixed AAIW was found at intermediate waters (>800 m).

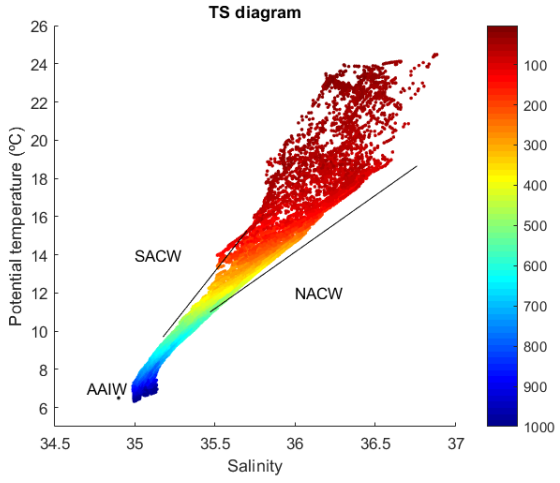


**Figure 2: TS diagram obtained from the ship CTD data. The SACW and NACW reference lines are taken from Tomzack (1981). The AAIW point is taken from Pérez *et al*. (2001). Dots are coloured according to their depth.**

The salinity vertical section (Figure 3) obtained by Bio along its track, from the NW to the SE, shows the water column from the surface to 1000 m depth. The maximum salinity is found at the surface layer, with values around 37. Salinity decreases gradually with depth to reach the minimum values (~35) at approximately 800 m depth. The lateral structure shows a high variability. The main features found are the lateral intrusions of less saline SACW and more saline NACW. There are also other mesoscale and submesoscale features found, such as filaments from the African Upwelling System at the surface layer (0-100 m).

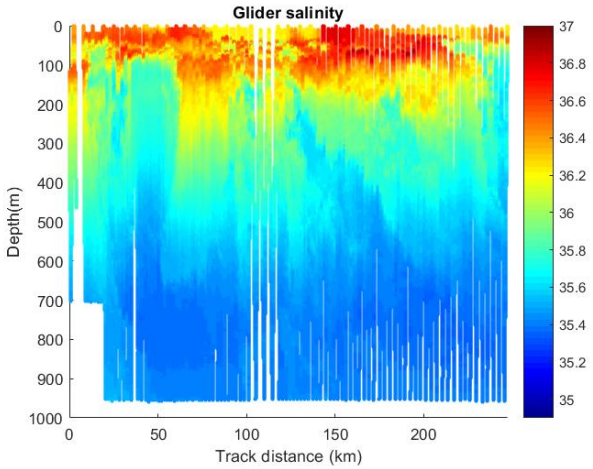


**Figure 3: Vertical section of the practical salinity obtained by the glider, along its south-eastward track.**

## 4.2. Wavelet analysis of synthetic signals

### 4.2.1. Wavelet analysis

The wavelet analysis is applied to the different datasets to analyse the scales that each sampling method and the Mercator model output can access, in order to compare the different sampling methods.

Our analysis uses distance as the independent variable rather than time, since our data does not consist on time series but are extracted from spatial sections. The wavelet analysis allows us to determine objectively the scales present in the analysed signal. It has been used with all the different data sources: gliders, SeaSoar, ship CTD and the Mercator model outputs.

### 4.2.2. Synthetic signals

Firstly, the analysis is performed on synthetic sinusoidal signals, to get familiar with the results and their interpretation in terms of the scales resolved and the power associated to them. To do so, 3 artificial signals were created using cosine-wave functions, to simulate the features found in the studied signals. They are constructed as:

$$y = \mathrm{A}_1 * \cos(k_1 * x) + \mathrm{A}_2 * \cos(k_2 * x) \ldots + A_n * \cos(k_n * x)$$

$$k = (2 * \pi)/L$$

where $A_i$ are the amplitudes of the signal, $k_i$ are the wavenumbers, and $L$ are the corresponding wavelengths.

Signals were created using a spatial resolution of 1 km, representing the distance between glider (1.2 km) and SeaSoar (2.5 km) consecutive profiles. Then, the signals were sub-sampled with a 10 km resolution, representing the model (11.5 km) and ship CTD (9.3 km) distance between profiles. The wavelet analysis was applied to both the original and the subsampled signals.

The selected wavelengths were: 7 km (L1), 12 km (L2), 25 km (L3) and 55 km (L4). L1 represents the submesoscale structures, probably lost in the 10 km resolution cases. L2 represents the mesoscale features. L3 is the size of the filaments and the smaller intrusions approximately. L4 represents the larger intrusions.

The output signals contain the different wavelengths.

- Signal 1 (Figure 4A) was built with L4 along the whole sampling length and represents the intrusions, which seem to be the main feature reported. Signal 1 has been also amplified from 0.3 to 30 to observe the result of the wave amplitude on the power of the signal obtained by the wavelet analysis.

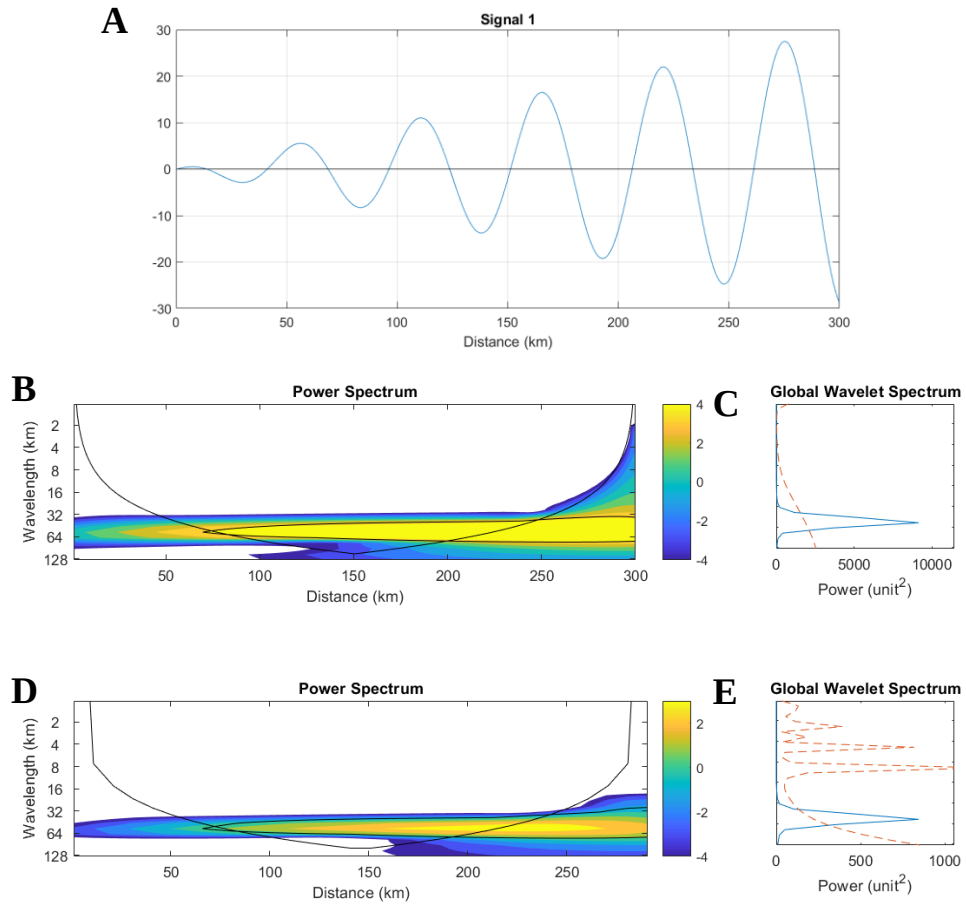


**Figure 4: (a) Output of the signal 1. Its amplitude increases from 0.3 to 30. It contains a 55 km wavelength. (b, d) Wavelet analysis and (c, e) Global spectrum of the signal 1, with the 1 (b, c) and 10 km (d, e) sampling resolution. The results on the area under the black line may be affected by edge effects. The black contour indicates the significant results. The Y and Z axis are logarithmic.**

Figures 4B and 4D show the wavelet results for signal 1. It shows a narrow wavelet, probably because only one wavelength is involved. As the amplitude increases, the power of the results and its width increase significantly. The 1 km and 10 km resolution samplings show similar results. This signal shows the highest energy. The energy is 10 times higher at the 1 km resolution sampling.

- Signal 2 (Figure 5A) represents the intrusions combined with the different structures. It was also built with a constant L4. From 1 to 100 km, L1 was added. Furthermore, from 100 to 125 km, L3 was added, and from 125 to 250 km, the wavelength goes from 25 km to 12 km (L3 to L2), to observe its effect on the results. Finally, from 200 to 300 km, L2 was added.

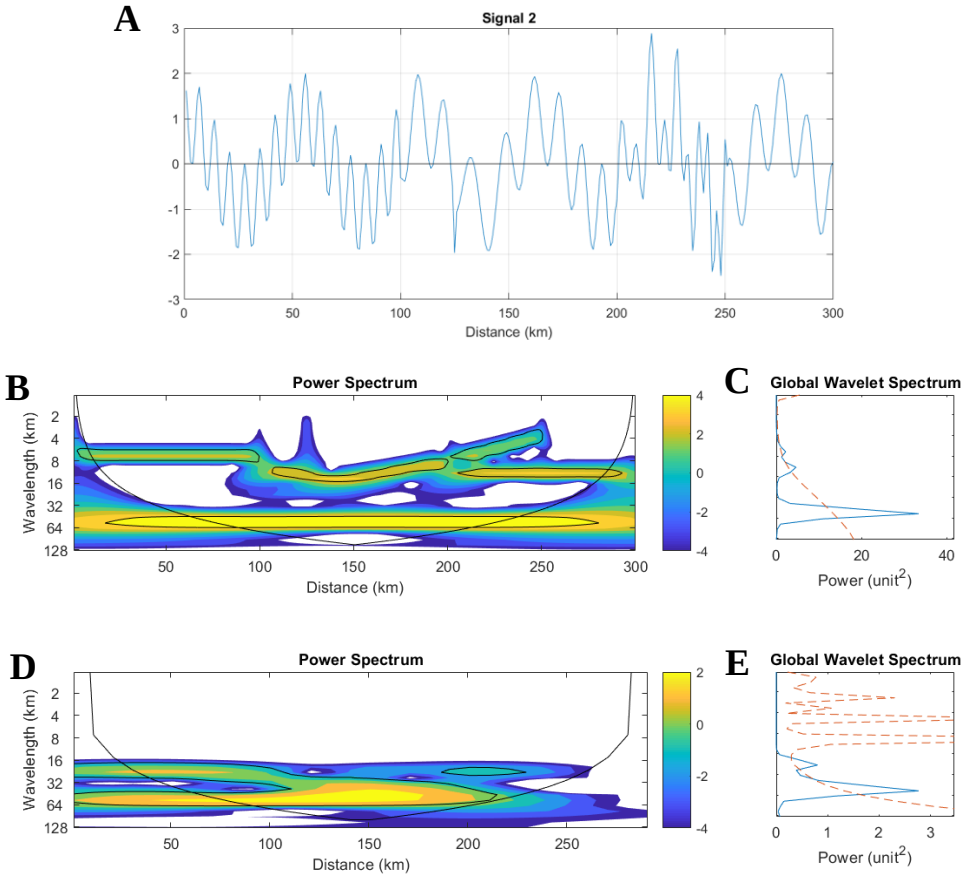


**Figure 5: (a) Output of the signal 2. It has a constant amplitude of 1. It is built as a combination of the 7, 12, 25 and 55 km wavelengths, with the 25 km wavelength decreasing progressively to 12 km. (b, d) Wavelet analysis and (c, e) Global spectrum of the signal 2, with the 1 (b, c) and 10 km (d, e) sampling resolution. The results on the area under the black line may be affected by edge effects. The black contour indicates the significant results. The Y and Z axis are logarithmic.**

Figures 6B and 6D show the wavelet results for signal 2. The 1 km resolution shows clearly the designed wavelengths, while the 10 km resolution result shows different wavelengths. L1 and L2 do not appear, due to the sampling resolution. At the 1 km resolution result the decrease from 25 to 12 km is shown; however, when it overlaps with the L2 the results are slightly distorted. The energy is approximately 10 times higher at the 1 km resolution.

- Signal 3 (Figure 6A) represents different combination of the features. It contains the L1, L2 and L4 wavelengths from 1 to 100 km, L1, L3 and L4 from 100 to 200 km, and L2, L3 and L4 from 200 to 300 km, respectively.

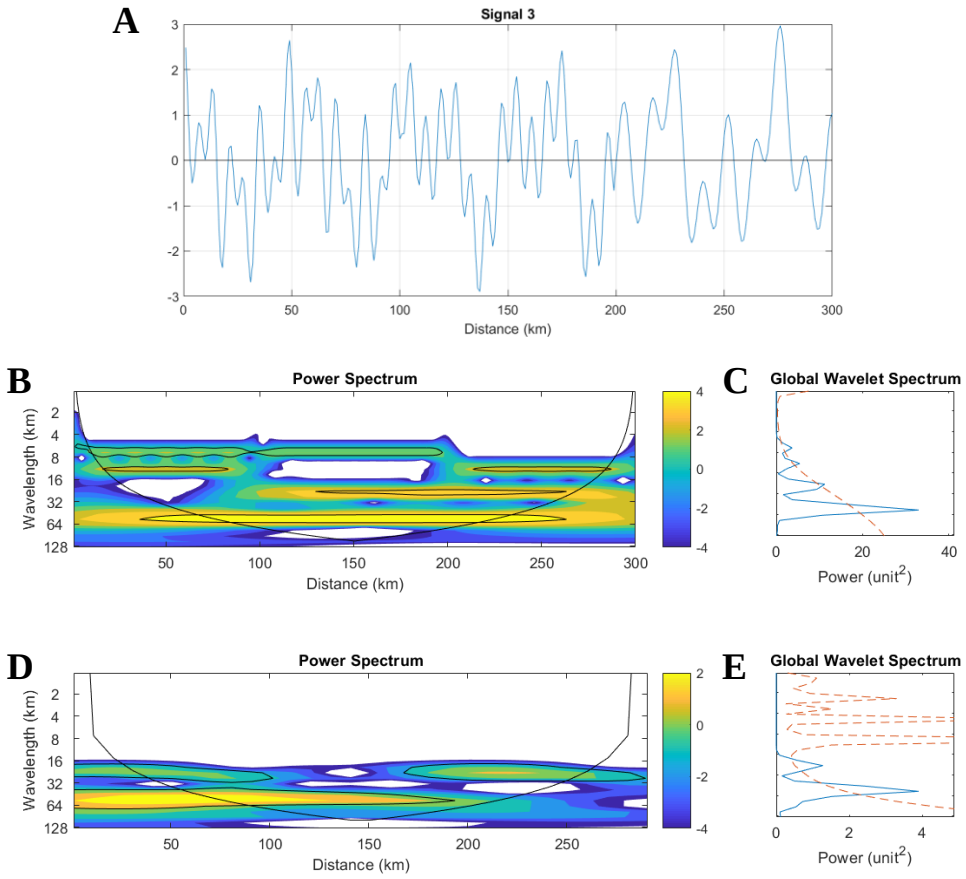


**Figure 6: (a) Output of the signal 3. It has a constant amplitude of 1. It is built as combinations of the 7, 12, 25 and 55 km wavelengths, at different parts of the signal. (b, d) Wavelet analysis and (c, e) Global spectrum of the signal 3, with the 1 (b, c) and 10 km (d, e) sampling resolution. The results on the area under the black line may be affected by edge effects. The black contour indicates the significant results. The Y and Z axis are logarithmic.**

Figures 6B and 6D show the wavelet results for signal 3. The 1 km resolution shows all the expected wavelengths. L1 and L2 are slightly overlapped when they are present at the same part of the signal, as L2 and L3. The 10 km resolution does not show the designed wavelengths. L1 and L2 are missing on the results. The energy is approximately 10 times higher at the 1 km resolution.

## 4.3. Wavelet analysis of in-situ signals

In order to create the time series, the datasets were sampled at a constant depth of 150, 350 and 600 m (the SeaSoar did not sample deeper that 400 m). The 150 m depth is a key location as the front is defined by the location of the 36 isohaline at 150 m depth (Zenk *et al.*, 1991). The other two depths are taken to explore the variability with depth of the features observed. All the series are taken at the same latitudinal range, so they cover the same area assuming that the features found should be the same, regardless of the

observation methodology considered. They are oriented from NE (left) to SW (right). The final signal is some 200 km across the CVFZ.

The spatial resolution of each method, calculated as the mean distance between two consecutive profiles for each method, is shown in Table 1.

**Table 1: Horizontal resolution of the different sampling methods.**

| Sampling method | Spatial resolution (km) | Sampling period (days) |
|---|---|---|
| Glider | 1.2 | 17 |
| SeaSoar | 2.5 | 1 |
| Ship CTD | 9.3 | 5 |
| Mercator model | 11.5 | - |

### 4.3.1. 150 m

At 150 m the temperature ranges between 13.5 and 17.5 ºC (Figure 7). Overall, there is no increasing or decreasing trend along the series.

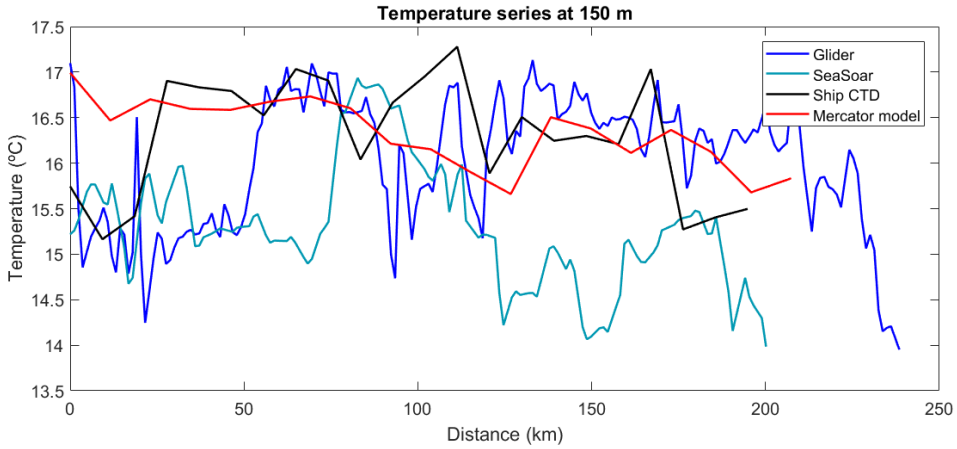


**Figure 7: Temperature from the glider, SeaSoar, ship CTD and Mercator model at 150m, starting at the NE (left) and finishing at the SW (right).**

The model sampling shows a slightly decreasing trend. At 125 km there is a sudden increase in temperature, with a size of 75 km. The ship CTD data shows variability without a clear trend. However, there is a sharp decrease at both edges and higher values at the centre of the track.

In the SeaSoar sampling there is a slightly decreasing trend. It is found an increase in temperature at the middle of the track (75 km) followed by a decrease (125 km). The SeaSoar shows higher frequency variability than the Mercator model and the ship CTD. The glider samplings show the highest variability, without a decreasing or increasing trend. It increases at the middle of the track (between 50-225 km).

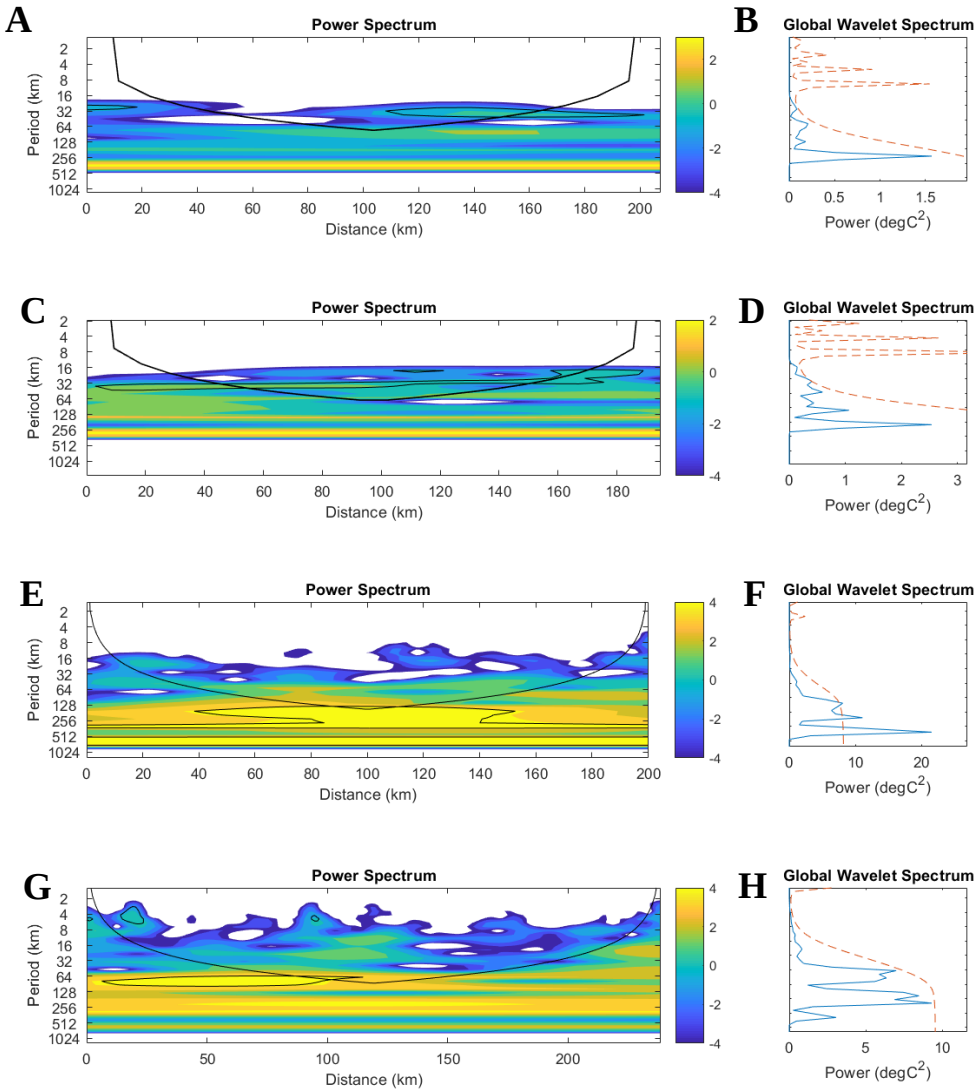


**Figure 8: (a, c, e, g) Wavelet analysis and (b, d, f, h) Global spectrum from the model (a, b), ship CTD (c, d), SeaSoar (e, f) and glider (g, h) at 150 m. The wavelet results on the area under the black line may be affected by edge effects. The black contour indicates the significant results. The Y and Z axis are logarithmic. The signals start at the NE (left) and finish at the SW (right).**

The Mercator model captures scales from 16 km to <500 km (Figure 8A, Table 2). The scales between 16 and 64 km are not constant during the whole track. There is a significant scale of approximately 32-16 km, between 0-20 km and 100 km until the end.

The ship CTD captures scales from 16 to ~200 km (Figure 8C). At the beginning of the signal the range is narrower, and it broadens towards the end of the signal, capturing smaller scales. There is a significant scale of 32 km. It starts at 32 km at the beginning

The SeaSoar captures scales from 4 to ~1000 km (Figure 8E). However, the ones smaller than 32 km appear intermittently. There is a constant significant scale of 512-1024 km, and of ~300 km. Between 40 and 140 km a significant scale of 128-300 km appears.

The glider captures scales from 2 km to ~1000 km (Figure 8G). The scales smaller than 16 km are not constant during the track. A significant scale around 4 km is found at some points at the beginning and the middle of the track. There is also a significant scale

between 60-100 km found at the beginning and middle of the track, with a constant presence.

The glider captures the broadest range of scales, while the model and the ship CTD capture the narrowest range. The glider and the SeaSoar have the highest amount of significant scales and the highest spatial variability. The SeaSoar shows the highest energy (20 $ºC^2$ at the peak), followed by the glider (10 $ºC^2$), the ship CTD (3 $ºC^2$) and the model (1.5 $ºC^2$) (Figures 8B, 8D, 8F and 8H).

### 4.3.2. 350 m

The temperature signal at 350 m is in the range 11.5-14 ºC (Figure 9). There is a decreasing trend on the series as it approaches the African coast.

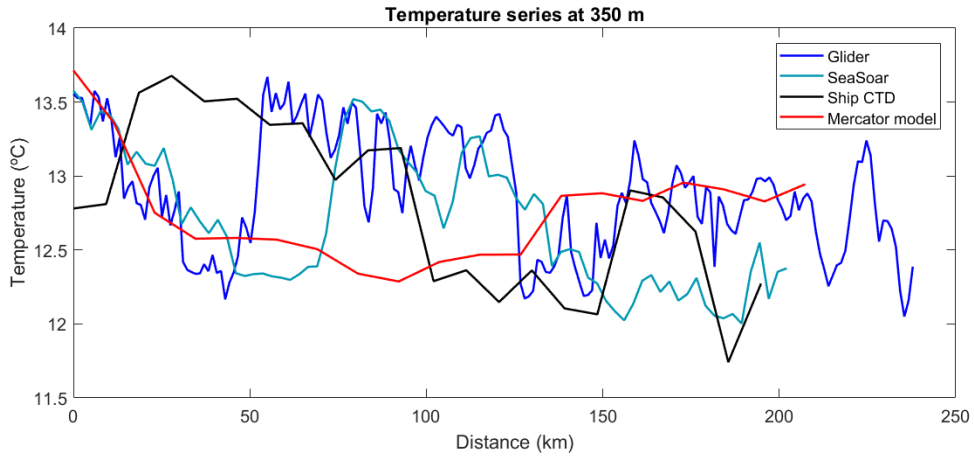


**Figure 9: Temperature from the glider, SeaSoar, ship CTD and Mercator model at 350m, starting at the NE (left) and finishing at the SW (right).**

The model sampling shows lower temperatures at the middle of the track and higher temperatures on the edges. It shows the least variability. The ship CTD shows a sudden increase at the beginning (25 km), decrease at 100 km and increase at 150-175 km.

The SeaSoar has a decreasing trend, but at 75 km there is an increase in temperature. It shows the highest slope. Both SeaSoar and glider show the highest variability. The glider shows abrupt changes at 50 km and 125 km.

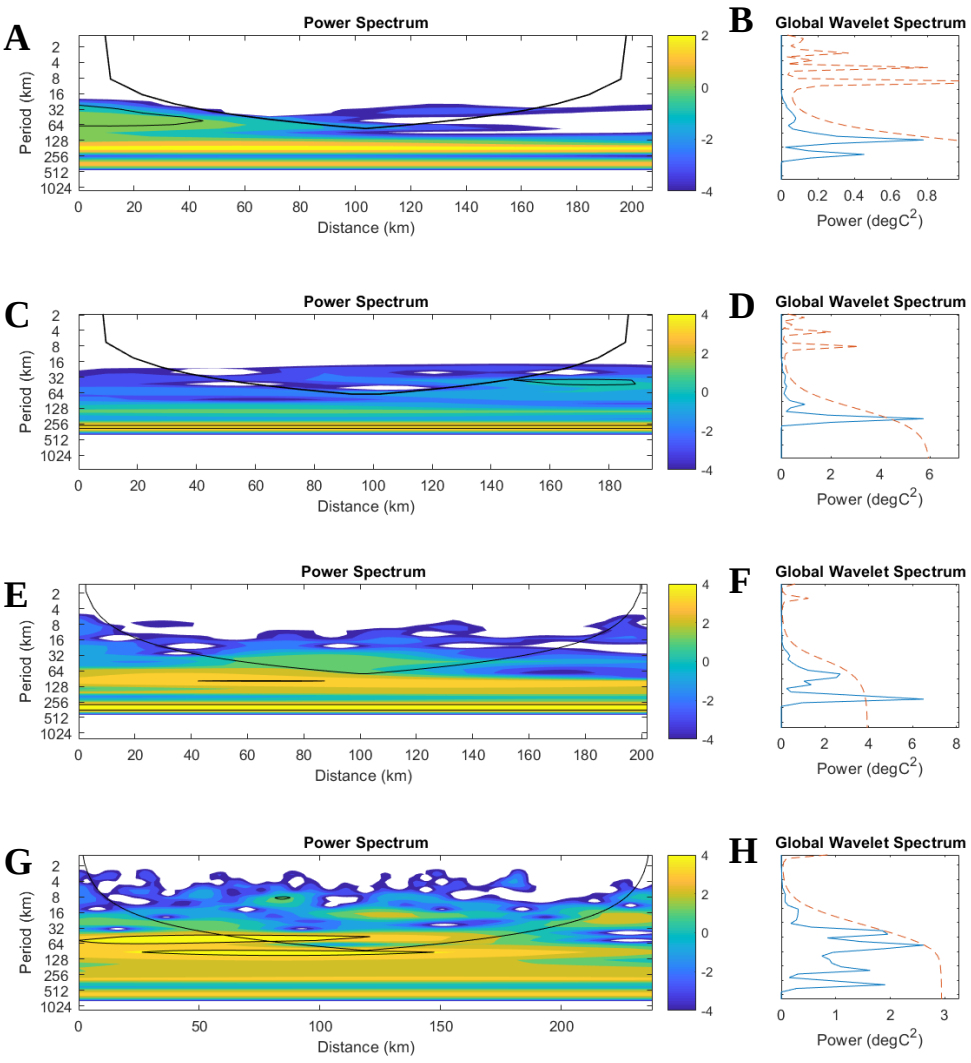


**Figure 10: (a, c, e, g) Wavelet analysis and (b, d, f, h) Global spectrum from the model (a, b), ship CTD (c, d), SeaSoar (e, f) and glider (g, h) at 350 m. The wavelet results on the area under the black line may be affected by edge effects. The black contour indicates the significant results. The Y and Z axis are logarithmic. The signals start at the NE (left) and finish at the SW (right).**

The Mercator model captures scales between 16 km and 512 km (Figure 10A). At the second part of the track the scales between 16 and 64 km disappear. There is a significant scale between 32-64 km at the beginning of the track.

The ship CTD shows scales between 16 and 512 km (Figure 10C). The range broadens slightly towards the end of the track on the smaller scales. However, the scales smaller than 64 km are not constant. There is a significant scale of 256 km, and, at the end of the signal (140-180 km) the 32 km scale is also significant.

The SeaSoar captures scales between 4 and 512 km (Figure 10E). The range is constant during all the signal, but the scales smaller than 32 km are intermittent. The 256 km scale is significant in the whole domain. Between 40 and 100 km the ~100 km scale is also significant.

The glider shows scales between 2 and 1024 km (Figure 10G). At the final part of the signal (>175 km) the range narrows to 4-1024 km. There is a significant scale of ~8 km

at 75 km. At the first middle of the signal (< 150 km) the scales 32-64 and 64-128 km are significant.

The model and the ship CTD show the narrowest range of scales and the glider shows the broadest. The glider and the SeaSoar show more spatial variability. The glider has the highest amount of significant scales. The SeaSoar and ship CTD show the highest energy (6 $ºC^2$ at the peak), followed by the glider (3 $ºC^2$), and the model (0.8 $ºC^2$) (Figures 10B, 10D, 10F and 10H).

### 4.3.3. 600 m

The temperature at 600 m ranges between 8.5 and 10.5 ºC (Figure 11). There is not a general increasing or decreasing trend in all the methods.

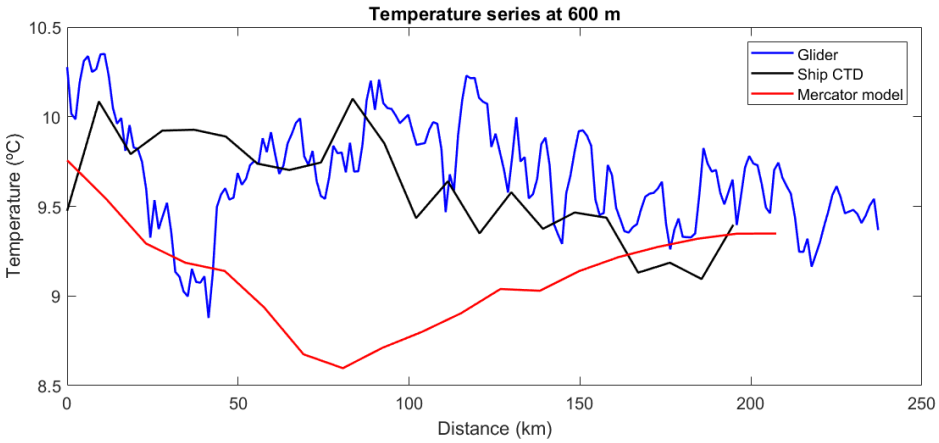


**Figure 11: Temperature from the glider, SeaSoar, ship CTD and Mercator model at 600m, starting at the NE (left) and finishing at the SW (right).**

The model sampling shows the lowest temperatures. The temperature decreases progressively at the centre of the signal. The ship CTD shows higher variability than the model, with a decreasing trend. The glider shows the highest variability. The temperature shows a pronounced lower peak at 50 km, and, generally, has a decreasing trend.

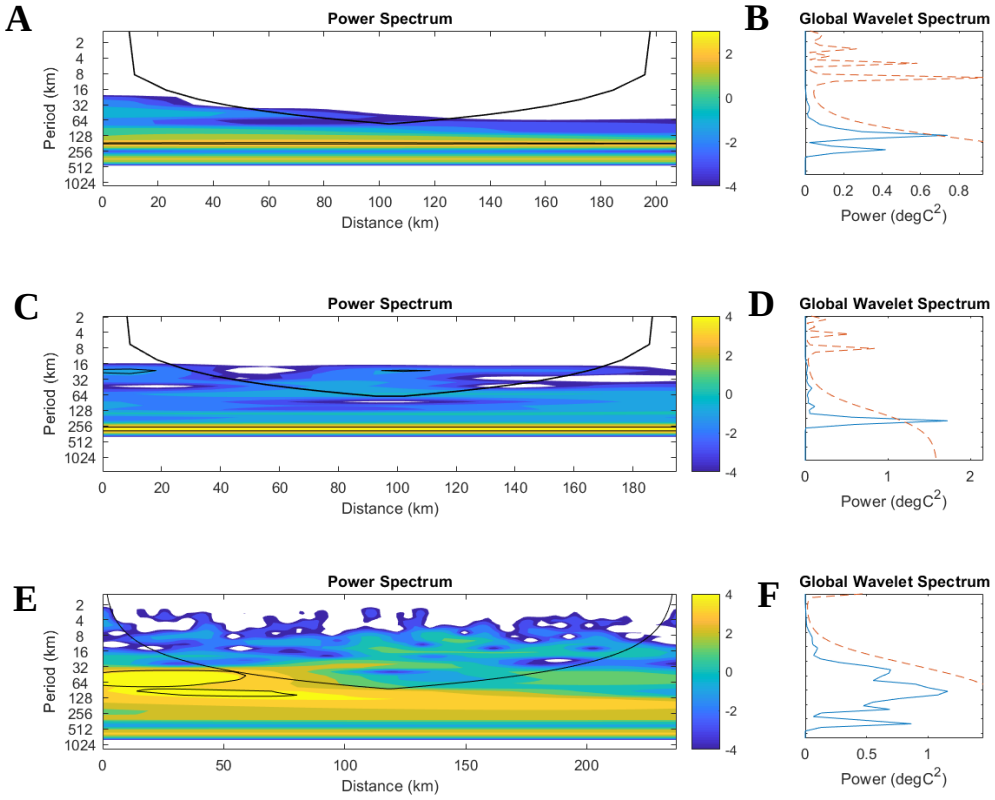


**Figure 12: (a, c, e) Wavelet analysis and (b, d, f) Global spectrum from the model (a, b), ship CTD (c, d) and glider (e, f) at 600 m. The wavelet results on the area under the black may be affected by edge effects. The black contour indicates the significant results. The Y and Z axis are logarithmic. The signals start at the NE (left) and finish at the SW (right).**

The Mercator model sampling shows scales between ~20 km and 512 km initially (Figure 12A). At the end of the signal, near the African coast, the range narrows to 64-512 km. There is a significant scale of ~20 km.

The ship CTD captures scales from 16 to 500 km (Figure 12C). The 16-32 km scales are not present constantly during the signal. The 256 km scale is significant at all the signal. The 16-32 km scale is significant at some parts of the track (0-20 km and 80-100 km).

The glider shows scales between 2 and 1024 km (Figure 12E). The scales between 2 and 16 km are present intermittently. There are two significant scales, at the beginning of the signal (<75 km), 32-64 km and 64-128 km.

The broadest range of scales is at the glider sampling, and the narrowest at the model's sampling. The glider also shows the highest spatial variability. The signal with the highest energy is the ship CTD (2 $^oC^2$), and the lowest energy belongs to the model (0.8 $^oC^2$). The glider shows an energy of 1 $^oC^2$ (Figures 12B, 12D and 12F).

**Table 2: Scale ranges and energies captured by each method at each depth**

| | Mercator model | | Ship CTD | | SeaSoar | | Glider | |
|---|---|---|---|---|---|---|---|---|
| | **Range of scales (km)** | **Max. energy ($^oC^2$)** | **Range of scales (km)** | **Max. energy ($^oC^2$)** | **Range of scales (km)** | **Max. energy ($^oC^2$)** | **Range of scales (km)** | **Max. energy ($^oC^2$)** |
| **150 m** | 16-512 | 1.5 | 16-256 | 3 | 4-1024 | 20 | 2-1024 | 10 |
| **350 m** | 16-512 | 0.8 | 16-512 | 6 | 4-512 | 6 | 2-1024 | 3 |
| **600 m** | 16-512 | 0.8 | 16-512 | 2 | - | - | 2-1024 | 1 |

The glider seems to be capturing the smallest scales, followed by the SeaSoar (Table 2). The Mercator model shows the least small scales. The highest energy is found by the SeaSoar, followed by the glider. The lowest energy is from the Mercator model. These results are consistent with the spatial resolution of each method. The maximum energy found decreases with depth for all the methods. This might be due to a lower variability at greater depths.

Table 1 shows the duration of the sampling of each method. The SeaSoar has the least duration, so it gives the closest approach to a synoptic view. The glider has the longest sampling time. A long sampling time can affect the results by the changing the oceanographic conditions between the beginning and the ending of the sampling.

## 4.4. Vertical sections

### 4.4.1. Mercator model

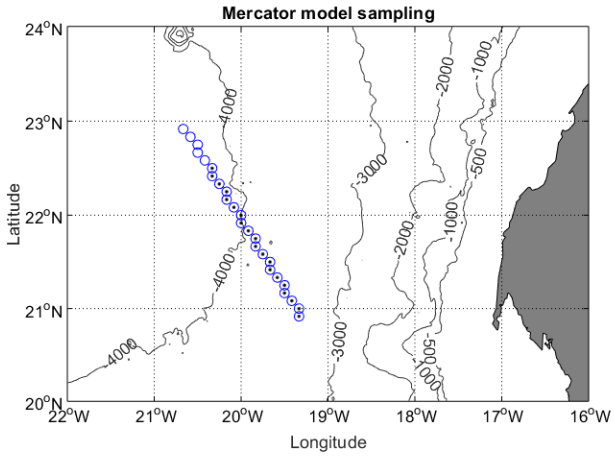


**Figure 13: Model points sampled. The blue circles indicate all the sampled points and the black dots the stations used on this comparison. The grey contour indicates the bathymetry of the area.**

The model data is selected according to the latitude and longitude range from the glider, and its temporal range (Figure 13). The sampling used the same days as the glider, starting at the north on November 4$^{th}$ and finishing at the south on November 21$^{st}$. It reaches 5500 m depth, but for this analysis it was used up to 1000 m.

The temperature ranges from 6 to 25 ºC and the salinity from 34.9 to 37 (Figures 14A and 14B).

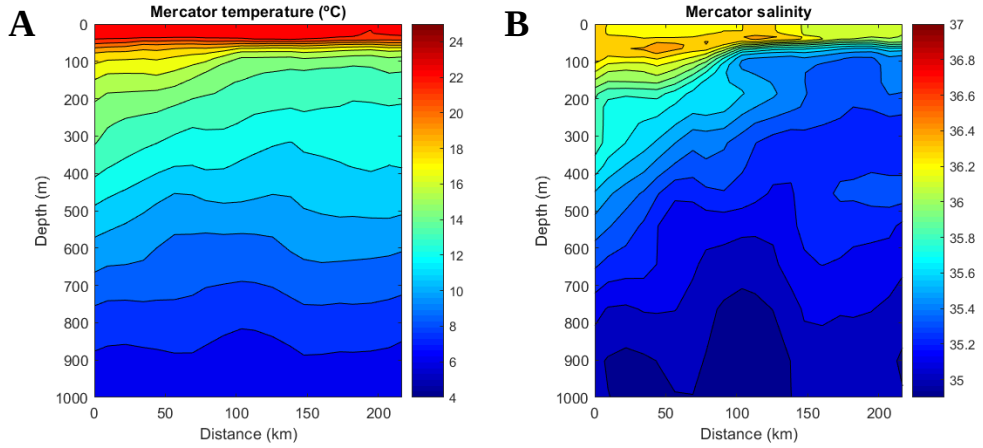


**Figure 14: Vertical section of the potential temperature (left) and salinity (right) obtained by the Mercator model, on the same location than the other sampling methods.**

The temperature distribution (Figure 18) seems stratified and does not show any clear features. The salinity distribution (Figure 19) shows more variations. At the first half of the track there is a more saline water at the surface layer, and the temperature is constant at this layer during the whole sampling.

### 4.4.2. Ship CTD

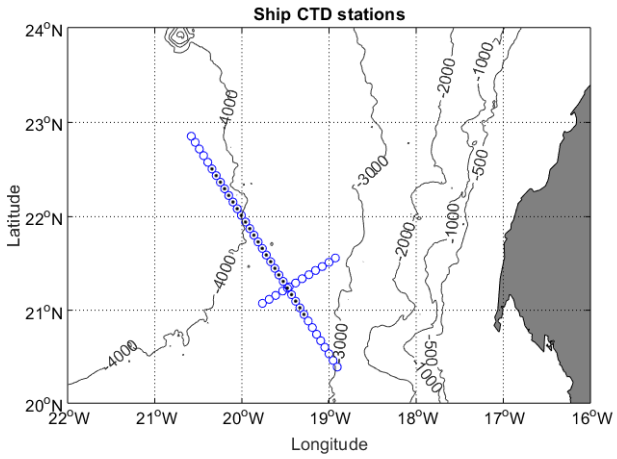


**Figure 15: Stations done by the ship, starting south and finishing on the north. The blue circles indicate all the stations and the black dots the stations used on this comparison. The grey contour indicates the bathymetry of the area.**

The ship performed 36 stations from 20.5ºN to almost 23ºN, separated 9.5 km between them (Figure 15). It started on November 11$^{th}$ to November 16$^{th}$ and finished on November 19$^{th}$ to November 20$^{th}$. It reached 1500 m depth, but for this project it was used until 1000 m.

The temperature ranges from 4.5 to 24.5 ºC and the salinity from 34.9 to 36.9 (Figures 16A and 16B).

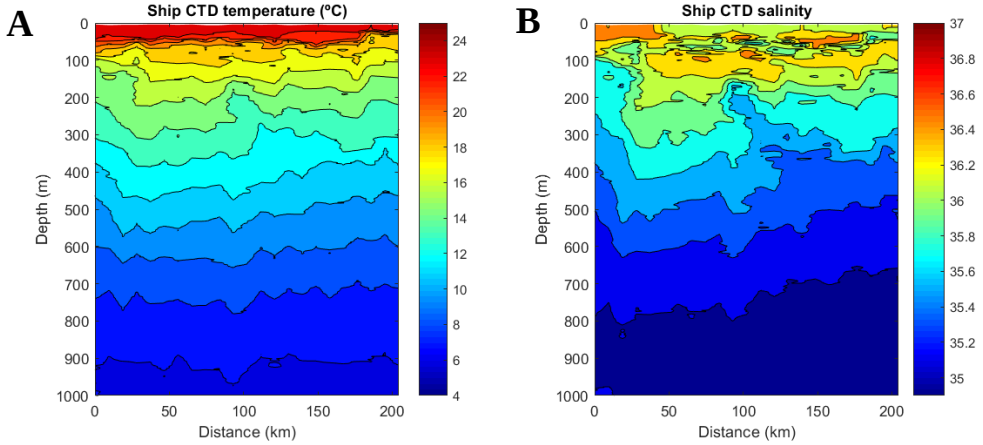


**Figure 16: Vertical section of the potential temperature (left) and salinity (right) obtained by the ship CTD along its track. It is oriented from north to south.**

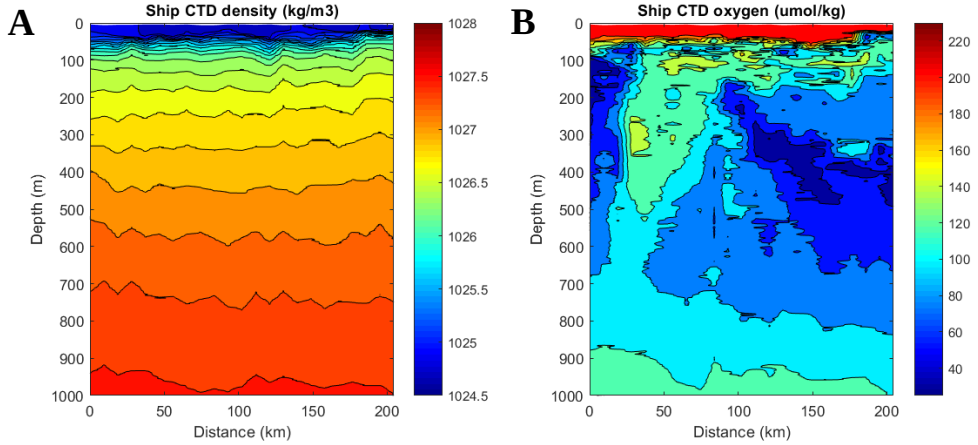


**Figure 17: Vertical section of the potential density (left) and dissolved oxygen concentration (right) obtained by the ship CTD along its track. It is oriented from north to south.**

The temperature and salinity distributions show some intrusions of SACW, colder and less saline than the NACW. They are found at 0-25 km and 100-150 km. The 100-150 km intrusion seems to be tilted. The intrusions seem to reach only 500 m depth.

The last 75 km (>200 km), at the highest latitude, show a more saline water at the surface layer. The temperature in the surface layer is similar during all the track. The density distribution seems to be compensated, as the CVFZ is a compensating front (Figure 17A). The density ranges from 1024.5 to 1027.8 kg/m$^3$.

The oxygen vertical section (Figure 17B) shows the intrusions clearly, marked by a lower value of oxygen concentration. At the surface layer the oxygen concentration remains high during the whole track. The oxygen concentration ranges from 23 to 225 μmol/kg.

### 4.4.3. SeaSoar

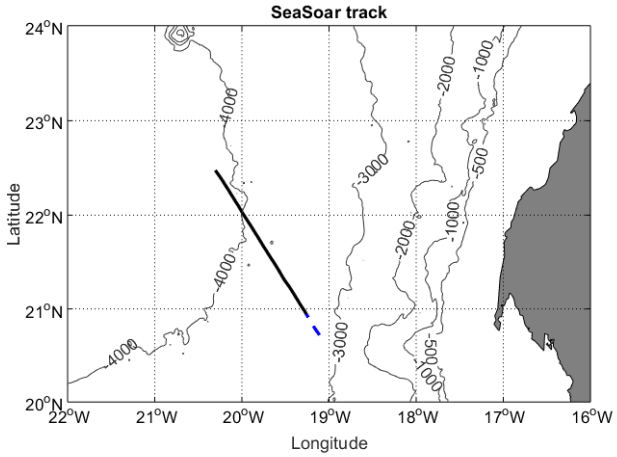


**Figure 18: Track followed by the SeaSoar on the T5, starting north and finishing on the south. The blue dotted line indicates the whole track, and the black line indicates the part used on this comparison. The grey contour indicates the bathymetry of the area.**

For this study, the transect T5 from the SeaSoar mesh was used. It started at the north and went southward (Figure 18), from November 8$^{th}$ to November 9th. The SeaSoar only reached 450 m depth.

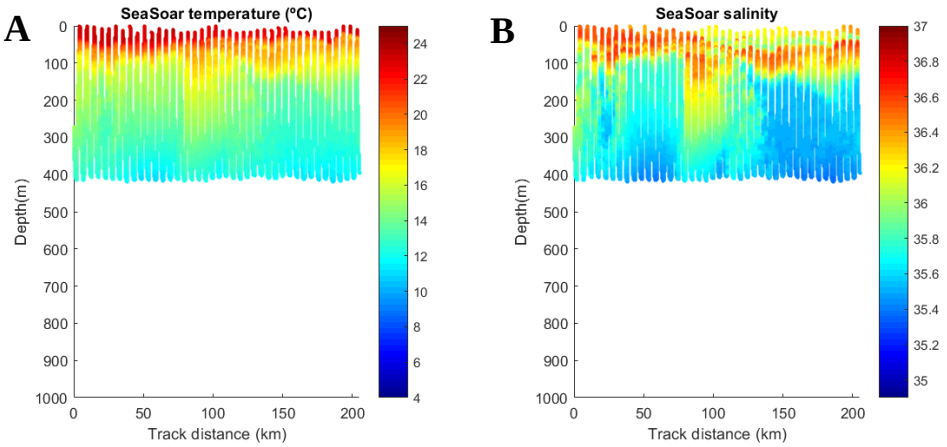


**Figure 19: Vertical section of the potential temperature (left) and salinity (right) obtained by the SeaSoar, along its track.**

The temperature ranges from 10 to 24 ºC and the salinity from 35.3 to 36.7 (Figure 19A and 19B). At the surface layer during the first 75 km the water is warmer and more saline than in the rest of the track.

The vertical sections show 3 intrusions of less saline and colder SACW, between 25-75 km, 125-175 km and >200 km. They might correspond with the intrusions in the ship CTD and glider vertical sections. The intrusions start at 100 m depth and reach the SeaSoar's maximum depth.

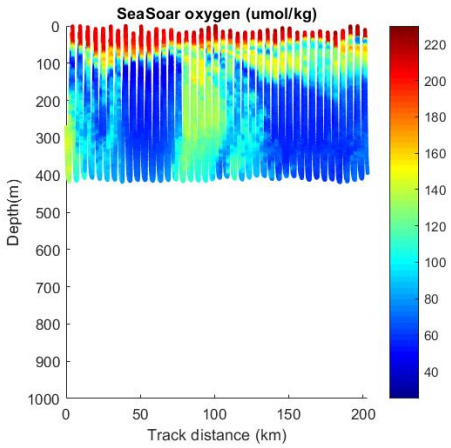


**Figure 20: Vertical section of the dissolved oxygen concentration obtained by the SeaSoar, along its track.**

The oxygen distribution (Figure 20) shows the same features than the salinity and temperature distributions, except for the surface layer. There is a high oxygen concentration at the surface during the whole track. The oxygen concentration ranges from 33 to 226 μmol/kg.

### 4.4.4. Glider

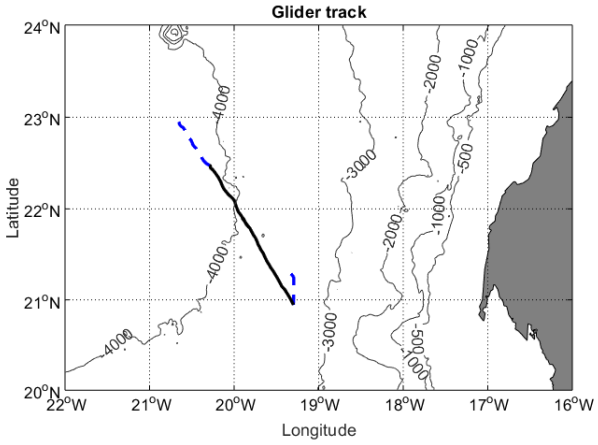


**Figure 21: Track followed by the glider, starting north and finishing on the south. The blue dotted line indicates the whole track, and the black line indicates the part used on this comparison. The grey contour indicates the bathymetry of the area.**

The glider started its southward track at 23ºN and turned back to the north at 21ºN (Figure 21). It dived from the surface to 1000 m depth. It started on November 4$^{th}$ and finished on November 21$^{st}$.

The temperature ranges from 6 to 25 ºC and the salinity from 35.3 to 37 (Figure 22A and 22B). There are high values of temperature at the surface layer at the whole section.

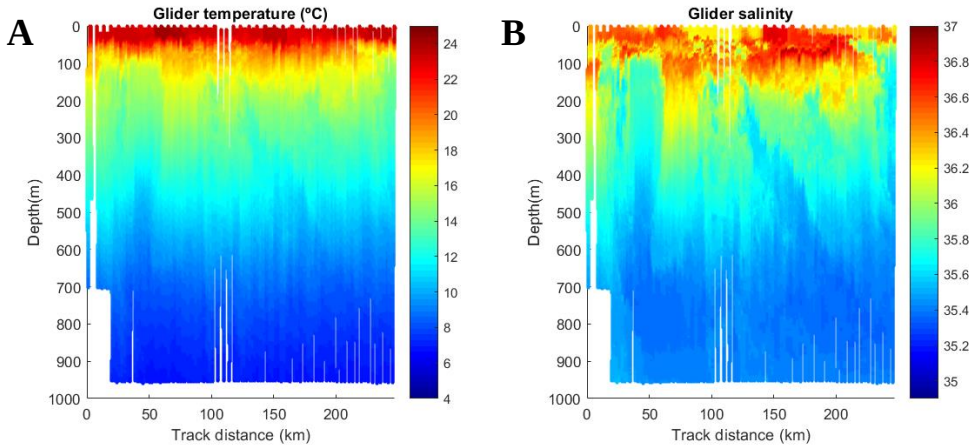


**Figure 22: Vertical section of the potential temperature (left) and salinity (right) obtained by the glider, along its track.**

The vertical sections show 3 large intrusions of SACW, between 25-50 km, 125-175 km and 225-250 km. The 2nd intrusion is strikingly tilted to the north. They seem to correspond with the same intrusions already described for SeaSoar and ship CTD data. As shown in the wavelet analyses, the glider shows them with greater detail. The intrusions seem to be located between 100 and 800 m depth.

The glider, SeaSoar and ship CTD show the same features, but the ship CTD result is coarser, as previously proven with the wavelet analyses.

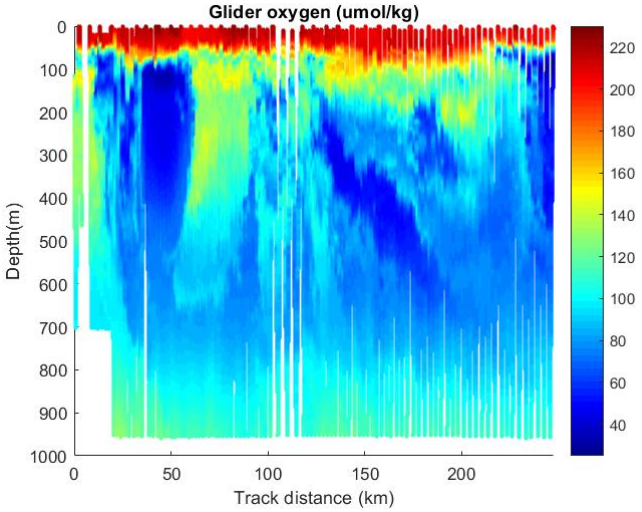


**Figure 23: Vertical section of the dissolved oxygen concentration obtained by the glider, along its track.**

The oxygen distribution (Figure 23) shows the same intrusions that the salinity and temperature distributions. The less saline and colder SACW intrusions are found in lower oxygen concentrations. The oxygen concentration ranges from 25 to 228 μmol/kg.

### 4.4.5. Tilted intrusion

A final section is devoted to the tilted intrusion, as this is considered to be one of the main novel aspects in this analysis. This feature would likely be missed if only data from the ship CTD or SeaSoar had been used. A high spatial rate sampling is needed to interpret

that signal as a coherent oceanographic structure. The tilted intrusion seems to begin at greater depths than the vertical ones. This might indicate that it was originally a vertical intrusion, tilted due to another phenomenon.

Figure 24 shows how the Mercator model captures the temporal evolution of an anticyclonic eddy at the front, shown in salinity maps at 200 m. We believe that the dynamic associated to this anticyclonic eddy might be the cause of the tilting of the intrusion. That eddy was described previously by Navarro *et al*. (2018).

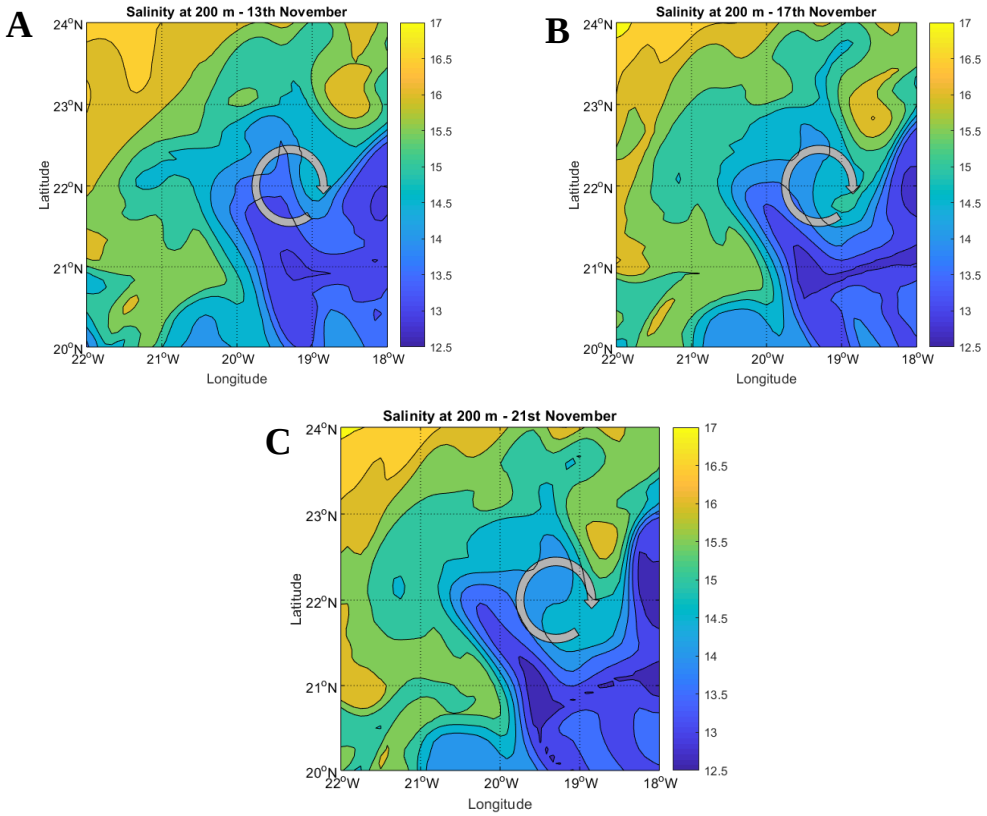


**Figure 24: Temporal evolution of the eddy found during the sampling, at the days (a) November 13th, (b) November 17th and (c) November 21st. The data is taken from the Mercator model, at 222.5 m depth. The arrow indicates the location of the eddy.**

## 5. Conclusions

1- The glider and the SeaSoar capture the smallest scales and, in consequence, the features are displayed with greater detail. The main advantage of the glider is its independence from the ship, allowing it to follow a different path than the cruise, if needed

2- The glider shows the finest spatial resolution on the horizontal, while at vertical scales the SeaSoar has the finest resolution. The ship CTD reaches the greatest depth of all the sampling methods, while the SeaSoar is the fastest method. The

high complexity of the CVFZ requires fast sampling methods with a high vertical and horizontal resolution, in order to represent it more accurately.

3- The wavelet analysis is proven to be a useful tool for comparing the resolution and the scales that each method can capture, in order to determine which one is the most helpful in different sampling strategies, according to the scientific objective.

4- The high-resolution sampling allows us to define the CVFZ as a dynamically complex front, with many hydrographic processes involved. The surface layer shows the highest variability, due to the interaction with the atmosphere and the upwelling filaments. The main features found are the intrusions of the less saline and colder SACW, with a minimum in oxygen concentration, into the more saline and warmer NACW.

5- It was found a new striking feature consisting on a tilted lateral intrusion, located at slightly greater depths than the other intrusions. It might be due to the deformation of a previously existing vertical intrusion, caused by the dynamics associated to an anticyclonic eddy. This intrusion could be captured by using the glider data, and the numerical model allowed us to establish the relationship between the intrusion and the eddy temporal evolution.

## 6. Acknowledgements

I would like to thank all the FLUXES-II team for providing all the data needed for this TFM, especially Ángeles Marrero, Carmen Gordo, Nadia Burgoa and Antonio González Ramos.

# 7. References


1. Bachmayer, R., Leonard, N., Graver, J., Fiorelli, E., Bhatta, P & Paley, D. (2004). Underwater Gliders: Recent developments and future applications. *Proceedings Of The 2004 International Symposium On Underwater Technology (IEEE Cat. No.04EX869)*, 195-200.
2. Bachmayer, R., de Young, B., Williams, C., Bishop, C., Knapp, C. & Foley, J. (2006). Development and Deployment of Ocean Gliders on the Newfoundland Shelf. *Proceedings of the Unmanned Vehicle Systems Canada Conference 2006*, Montebello, Canada.
3. Baker, J. W. (2007). Quantitative classification of near-fault ground motions using wavelet analysis. *Bulletin of the Seismological Society of America*, 97(5), 1486-1501.
4. Baliunas, S., Frick, P., Sokoloff, D., & Soon, W. (1997). Time scales and trends in the central England temperature data (1659–1990): A wavelet analysis. *Geophysical Research Letters*, 24(11), 1351-1354.
5. Barton, E. (1987). Meanders, eddies and intrusions in the thermohaline. *Oceanol. Acta*, 10(3), 267-283.
6. Bashmachnikov, I., Nascimento, A., Neves, F. & Menezes, T. (2015). Distribution of intermediate water masses in the subtropical northeast Atlantic. *Ocean Science Discussions*, 12, 769-822.
7. Combes, J. M., Grossmann, A., & Tchamitchian, P. (Eds.). (2012). Wavelets: Time-Frequency Methods and Phase Space. *Proceedings of the International Conference, Marseille, France, December 14–18, 1987*. Springer Science & Business Media.
8. Farge, M. (1992). Wavelet transforms and their applications to turbulence. *Annual review of fluid mechanics*, 24(1), 395-458.
9. Gao, W., & Li, B. L. (1993). Wavelet analysis of coherent structures at the atmosphere-forest interface. *Journal of Applied Meteorology*, 32(11), 1717-1725.
10. Gollmer, S. M., Cahalan, R. F., & Snider, J. B. (1995). Windowed and wavelet analysis of marine stratocumulus cloud inhomogeneity. *Journal of the atmospheric sciences*, 52(16), 3013-3030.
11. Grossmann, A., & Morlet, J. (1984). Decomposition of Hardy functions into square integrable wavelets of constant shape. *SIAM journal on mathematical analysis*, 15(4), 723-736.
12. Gu, D., & Philander, S. G. H. (1995). Secular changes of annual and interannual variability in the tropics during the past century. *Journal of Climate*, 8(4), 864-876.
13. Hagen, E. (1985). A meandering intermediate front North-West off Cape Verde islands. *Oceanogr. Trop*, 20, 71-83.
14. Hernández-García, I., González-Ramos, A. & Rodríguez-Santana, A. (2018). Validation of ocean forecasting model data with those obtained from the first transoceanic autonomous underwater vehicles (gliders) missions in the North-East

Atlantic basin (Trabajo de Fin de Grado). ULPGC, Las Palmas de Gran Canaria, España.

15. Hughes, P., & Barton, E. D. (1974). Stratification and water mass structure in the upwelling area off northwest Africa in April/May 1969. *Deep Sea Research and Oceanographic Abstracts* 21(8), 611-628.
16. Kumar, P., & Foufoula-Georgiou, E. (1993). A new look at rainfall fluctuations and scaling properties of spatial rainfall using orthogonal wavelets. *Journal of Applied Meteorology*, 32(2), 209-222.
17. Lau, K. M., & Weng, H. (1995). Climate signal detection using wavelet transform: How to make a time series sing. *Bulletin of the American meteorological society*, 76(12), 2391-2402
18. Liu, P. C. (1994). Wavelet spectrum analysis and ocean wind waves. *Wavelet Analysis and Its Applications*, 4, 151-166.
19. Martínez-Marrero, A., Rodríguez-Santana, A., Hernández-Guerra, A., Fraile-Nuez, E., López-Laatzen, F., Vélez-Belchí, P., & Parrilla, G. (2008). Distribution of water masses and diapycnal mixing in the Cape Verde Frontal Zone. *Geophysical Research Letters*, 35(7).
20. Martínez-Marrero, A., Arístegui, J., Rodríguez-Santana, A., Álvarez, X.A., & Delgado, A. (2017). Informe de la Campaña FLUXES II, 62pp.
21. Meyers, S. D., Kelly, B. G., & O'Brien, J. J. (1993). An introduction to wavelet analysis in oceanography and meteorology: With application to the dispersion of Yanai waves. *Monthly weather review*, 121(10), 2858-2866.
22. Mittelstaedt, E. (1983). The upwelling area off Northwest Africa---A description of phenomena related to coastal upwelling. *Progress in Oceanography*, 12, 307-331.
23. Morlet, J., Arens, G., Fourgeau, E., & Glard, D. (1982). Wave propagation and sampling theory—Part I: Complex signal and scattering in multilayered media. *Geophysics*, 47(2), 203-221.
24. Morlet, J. (1983). Sampling theory and wave propagation. *Issues in acoustic Signal—image processing and recognition*, 233-261.
25. Navarro, L., Martínez-Marrero, A. & Rodríguez-Santana, A. (2018). Hydrographical and dynamical properties of the Cape Verde Frontal Zone during the FLUXES-II survey (Trabajo de Fin de Grado). ULPGC, Las Palmas de Gran Canaria, España.
26. Pelegrí, J. L., Peña-Izquierdo, J., Machín, F., Meiners, C., & Presas-Navarro, C. (2017). Oceanography of the Cape Verde Basin and Mauritanian Slope Waters. *Deep-Sea Ecosystems Off Mauritania*, 119-153.
27. Pérez, F., Mintrop, L., Llinás, O., Glez-Dávila, M., Castro, C., Alvarez, M., ... & Ríos, A. (2001). Mixing analysis of nutrients, oxygen and inorganic carbon in the Canary Islands region. *Journal of Marine Systems*, 28, 183-201.
28. Pérez-Rodríguez, P., Pelegrí, J. L., & Marrero-Díaz, A. (2001). Dynamical characteristics of the Cape Verde frontal zone. *Scientia Marina*, 65(S1), 241-250.
29. Ramos, A. G., García-Garrido, V. J., Mancho, A. M., Wiggins, S., Coca, J., Glenn, S., ... & Haskins, T. (2018). Lagrangian coherent structure assisted path planning for transoceanic autonomous underwater vehicle missions. *Scientific reports*, 8(1), 4575.

30. Rudnick, D., Davis, R., Eriksen, C., Fratantoni, D. and Perry, M. (2004). Underwater gliders for ocean research. *Marine Technology Society Journal*, 38(1), 48-59.
31. von Schuckmann, K., Le Traon, P., Alvarez-Fanjul, E., Axell, L., Balmaseda, M., Breivik, L., ... & Verbrugge, N. (2016). The Copernicus Marine Environment Monitoring Service Ocean State Report. *Journal of Operational Oceanography*, 9(2), 235-320.
32. Tomczak Jr, M., & Hughes, P. (1980). Three-dimensional variability of water masses and currents in the Canary Current upwelling region. *Meteor Forschungsergeb., Reihe A*, 21, 1-24.
33. Tomczak Jr, M. (1981). An analysis of mixing in the frontal zone of South and North Atlantic Central Water off North-West Africa. *Progress in Oceanography*, 10(3), 173-192.
34. Torrence, C., & Compo, G. P. (1998). A practical guide to wavelet analysis. *Bulletin of the American Meteorological society*, 79(1), 61-78.
35. Venkata-Ramana, R., Krishna, B., Kumar, S. R., & Pandey, N. G. (2013). Monthly rainfall prediction using wavelet neural network analysis. *Water resources management*, 27(10), 3697-3711.
36. Wang, B., & Wang, Y. (1996). Temporal structure of the Southern Oscillation as revealed by waveform and wavelet analysis. *Journal of Climate*, 9(7), 1586-1598.
37. Weng, H., & Lau, K. M. (1994). Wavelets, period doubling, and time–frequency localization with application to organization of convection over the tropical western Pacific. *Journal of the atmospheric sciences*, 51(17), 2523-2541.
38. Zenk, W., Klein, B., & Schroder, M. (1991). Cape Verde frontal zone. *Deep Sea Research Part A. Oceanographic Research Papers*, 38, S505-S530.